The SMR results, in Table 3.10, indicate that planar failures yield a minimum value of 57, classifying the rock mass as Class III (normal quality, partially stable, requiring systematic stabilization). Toppling conditions generally reached values of 82, indicating Class I (very good quality, fully stable, no interventions required). Wedge failures mostly fell into Class II (good quality), with one case reaching Class I. However, localized intersections of discontinuities, such as S1–S2 on slope V1 and S1–S3 on slopes V1 and V2, produced much lower SMR values (22 and 32, respectively), corresponding to Class IV (poor quality) and indicating instability phenomena that would require extensive remedial measures.

Table 3.10: Results of the SMR method application for the three analyzed slopes (V1, V2, and V3). Critical values are marked with an asterisk.

Discontinuity System	**Planar Failure**			**Toppling**			**Intersection**	**Wedge Failure**		
	V1	V2	V3	V1	V2	V3		V1	V2	V3
Bedding	73	73	73	82	82	82	Bedding–S1	73	73	73
S1	57	57	57	82	82	82	Bedding–S2	73	75	81
S2	79	57	57	82	82	82	Bedding–S3	73	73	73
S3	57	72	79	82	82	82	S1–S2	22*	73	73
							S1–S3	32*	32*	75
							S2–S3	62	75	75

3.1.6.5 Rock slope statistical kinematic stability analysis

The analysis was conducted utilizing the data collected in-situ from the engineering-geological survey, the data sampled from the 3D point cloud, and considering the three slope orientations previously defined (representing the average slope trend and the local trends in pivotal areas).

The friction angle (φ) was defined for all the discontinuities systems as equal to 38° and it is coherent with the results obtained by the engineering-geology survey and the data

reported in the available literature for the area **(Geogar, 2015)**.

In Figure 3.17 is shown an example of the stereonet resulting from the **Markland Test (1972)** for the whole rock mass.

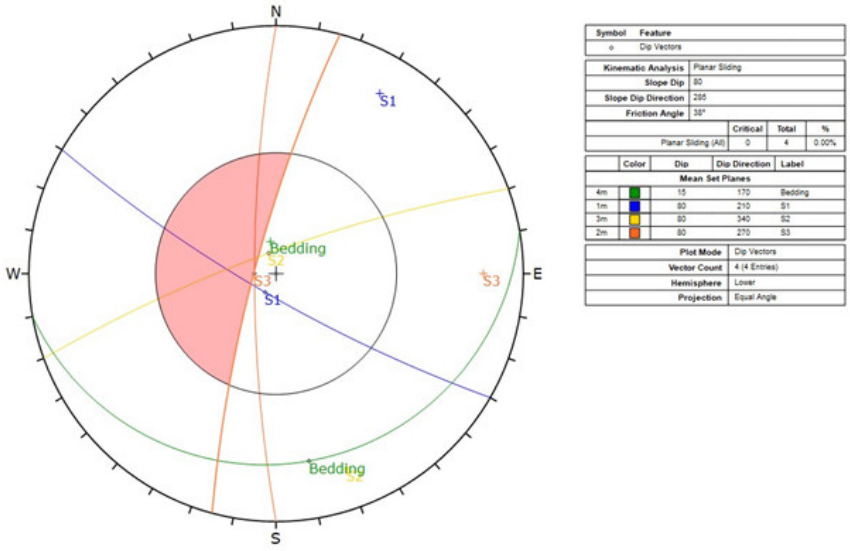

Figure 3.17: The image shows an example of the **Markland Test (1972)** conducted for slope V1 considering the planar sliding mechanism.

In Table 3.11, which summarizes the results obtained from the statistical kinematic stability analysis, based on the input data of Table 3.9, it can be already defined wedge sliding and direct toppling as the predominant kinematic mechanisms. Planar sliding only occurs in the case of slope V3 (210°/80°) and is related to the discontinuity system S1 (210°/80°) acting as sliding surface. The flexural toppling phenomenon has not been observed in the results, and it is usually considered as theoretically inconsistent with the limestones lithology.

Table 3.11: Results of the kinematic slope stability analysis.

Slope	**Planar sliding**	**Wedge sliding**	**Direct (DT) or Oblique toppling (OT)**
V1 (285°/80°)	–	S1–S2, S2–S3	DT bedding–S1 with S3 releasing plane
V2 (245°/80°)	–	S1–S2, S1–S3	OT with bedding as basal and releasing plane
V3 (210°/80°)	S1	S1–S3	OT S2–S3 with bedding and S1 as releasing planes

3.1.6.6 Deterministic kinematic and dynamic stability analysis

Among the few potentially unstable rock blocks identified on the slopes, this section focuses on blocks n.1 and n.2 (3.18, which are the most critical due to their larger volumes and proximity to the cave entrance and the archaeological areas of interest. Their main geometrical features, derived from the 3D point cloud, are summarized in Table 3.12.

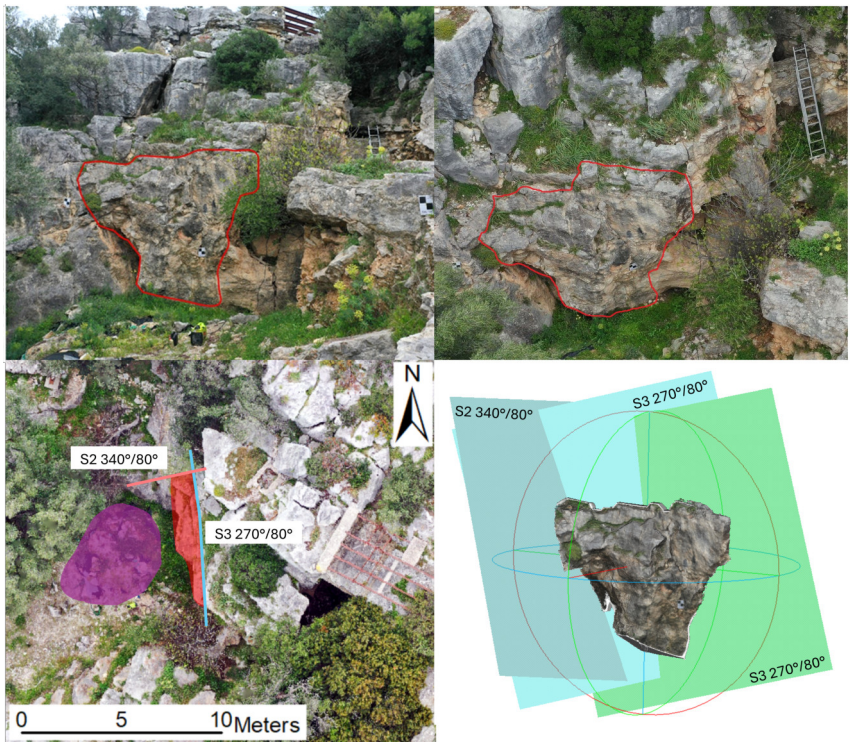

Figure 3.18: Panel (A) and (B) show Block n.1 in front and oblique views. Panel (C) highlights its position relative to the external archaeological excavation area (in purple), with the discontinuity systems that are creating a potentially unstable volume. Panel (D) shows the mesh obtained by CloudCompare software processing(Version 2; **CloudCompare, 2021**) and the planar discontinuities bordering it.

Table 3.12: Geometrical attributes of blocks n.1 and n.2 in terms of Dip Direction (DipDir) and Dip.

Block ID	**Volume (m^3)**	**J1 DipDir/Dip (°)**	**J2 DipDir/Dip (°)**	**J3 DipDir/Dip (°)**
1	14.59	93/88	82/89	186/70
2	17.73	124/81	5/78	269/14

The deterministic kinematic analysis conducted with Dips™ (Table 3.13) indicates that block n.1, located on slope V2, is mainly controlled by flexural toppling, with planar sliding also considered possible. Block n.2, on slope V1, shows combined instability mechanisms, with both direct/oblique and flexural toppling identified as relevant failure modes.

Table 3.13: Kinematic stability results for blocks n.1 and n.2.

Block ID	**Slope**	**Kinematic Mechanism**
1	V2	Planar sliding and Flexural toppling
2	V1	Direct/Oblique and Flexural toppling

The subsequent dynamic analysis of the two blocks was performed using RocTopple™ and RocPlane™ and Factors of Safety (FoS) are reported in Table 3.14 and Table 3.16.

Table 3.14: Deterministic dynamic analysis results of blocks n.1 and n.2 for direct/oblique and flexural toppling.

Block ID	**Kinematic mechanism**	**Standard FoS**	**Seismic FoS**	**Water filling FoS (limit)**	**Seismic + water FoS (limit)**
1	FT	6.74	4.59	2.74–0.1 (67–68%)	2.97–0.1 (52–53%)
2a	DT/OT	10.88	6.72	2.78–0.1 (68–69%)	3.09–0.1 (55–56%)
2b	FT	10.81	6.67	2.82–0.1 (66–67%)	3.14–0.1 (53–54%)

FoS = Factor of Safety; FT = Flexural toppling; DT = Direct toppling; OT = Oblique toppling. Values in parentheses indicate the percentage of joint water filling at limit equilibrium.

Table 3.16: Deterministic dynamic analysis results of Block n.1 for planar sliding.

Block ID	Slope	Standard Conditions FoS	Seismic Input FoS	Water Filling FoS (limit)	Seismic Input + Water FoS (limit)
1	V2	0.80	0.62	–	–

Block n.1 (FT) shows FoS values of 6.74 under standard conditions and 4.59 with seismic input. With water filling, FoS decreases from 2.74 at 67% to below 1 at 68%, while under seismic input and water filling, FoS shifts from 2.97 at 52% to instability at 53%.

Block n.2a (DT/OT) presents FoS values of 10.88 under standard conditions and 6.72 with seismic input. In the presence of water filling, FoS decreases from 2.78 at 68% to instability at 69%, while under seismic input combined with water, FoS shifts from 3.09 at 55% to instability at 56%.

Block n.2b (FT) yields FoS values of 10.81 under standard conditions and 6.67 with seismic input. With water filling, FoS decreases from 2.82 at 66% to instability at 67%, and under seismic input with water, FoS decreases from 3.14 at 53% to instability at 54%.

Planar sliding analysis with RocPlane^{TM} for Block n.1 on slope V2 indicates FoS values of 0.80 under standard conditions and 0.62 with seismic input.

3.1.6.7 Numerical modeling

Geotechnical models allowed for the evaluation of rock mass behavior and offered insights into the localization of stresses along the considered cross-sections. The distribution of differential stress ($\sigma_1 - \sigma_3$) around the cave is shown in Figures 3.19, 3.20, and 3.21. This parameter is crucial to understanding the structural response of the rock mass, as it permits the calculation of both shear and tensile stresses in the presence of jointed rocks and cavities.

Along the AA' cross-section (Figure 3.19), the highest differential stress values reach

up to 39 MPa, primarily localized at the intersections between bedding, joint sets, and the cave surface. Specifically, maximum values range from approximately 18 to 39 MPa.

The BB' cross-section (Figure 3.20) shows significantly lower stress magnitudes, with maximum values of 1.31 MPa concentrated where the S2 joint system intersects the cave surface. Here, differential stress varies between 0.87 and 2.90 MPa at the chamber edges.

Similar results were obtained along the CC' cross-section (Figure 3.21), where maximum differential stress ranges between 0.72 and 1.44 MPa.

Displacement analysis highlighted critical conditions only along the AA' cross-section. As shown in Figure 3.22, total displacement values reach approximately 5 cm, concentrated in the roof connecting the Atrium and Chamber 1, where the S1 discontinuity intersects the limestone bedding, generating potentially unstable geometries. In contrast, cross-sections BB' and CC' exhibit negligible displacement, generally below 1 mm. Figure 3.23 shows, as an example, the displacement field computed for the CC' cross-section.

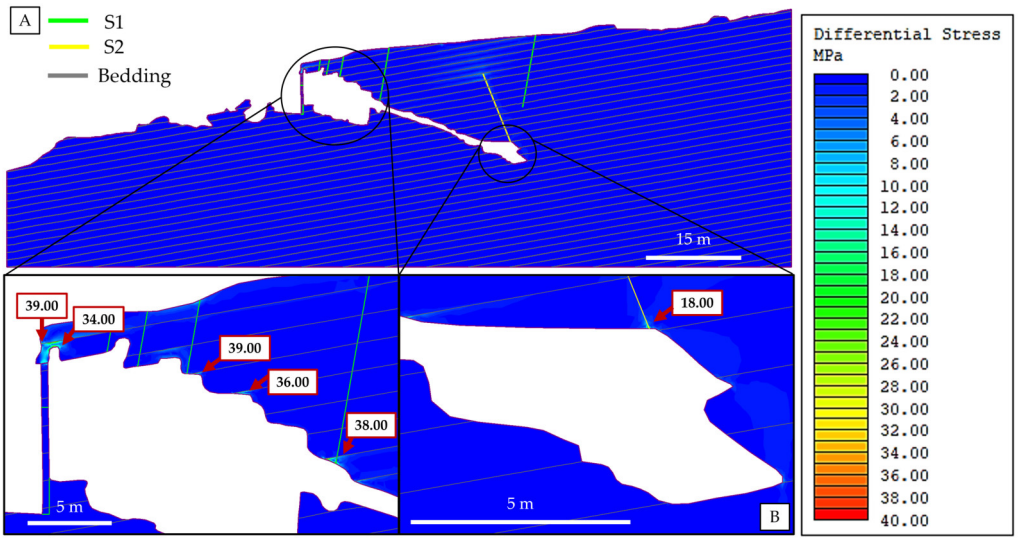

Figure 3.19: Differential stresses resulting from geotechnical modelling along the AA' cross-section (A). Details of the obtained differential stress values (B).

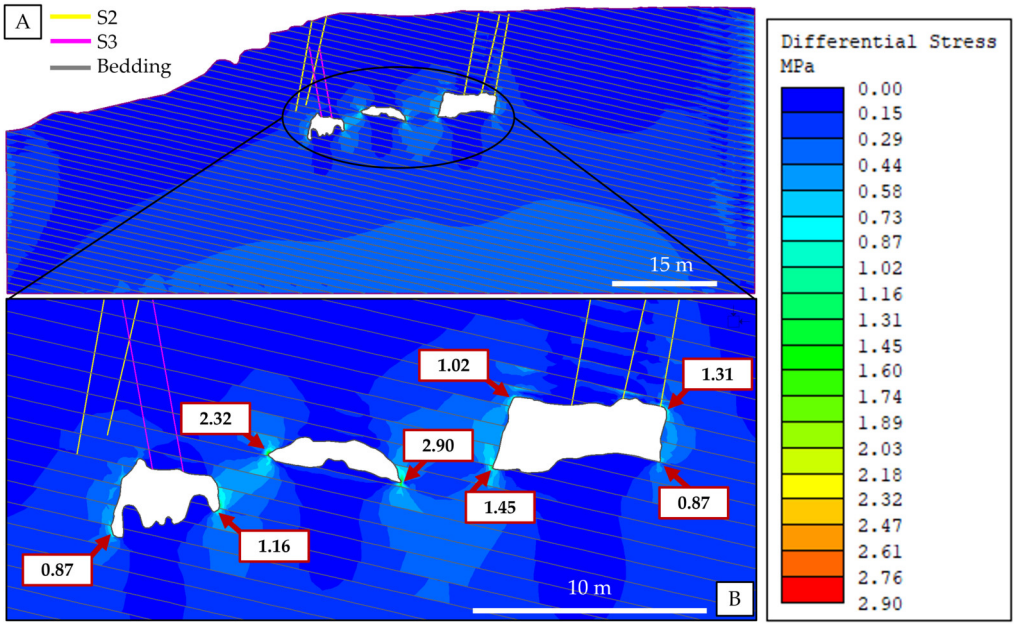

Figure 3.20: Differential stresses resulting from geotechnical modelling along the BB' cross-section (A). Detail of the obtained differential stress values (B).

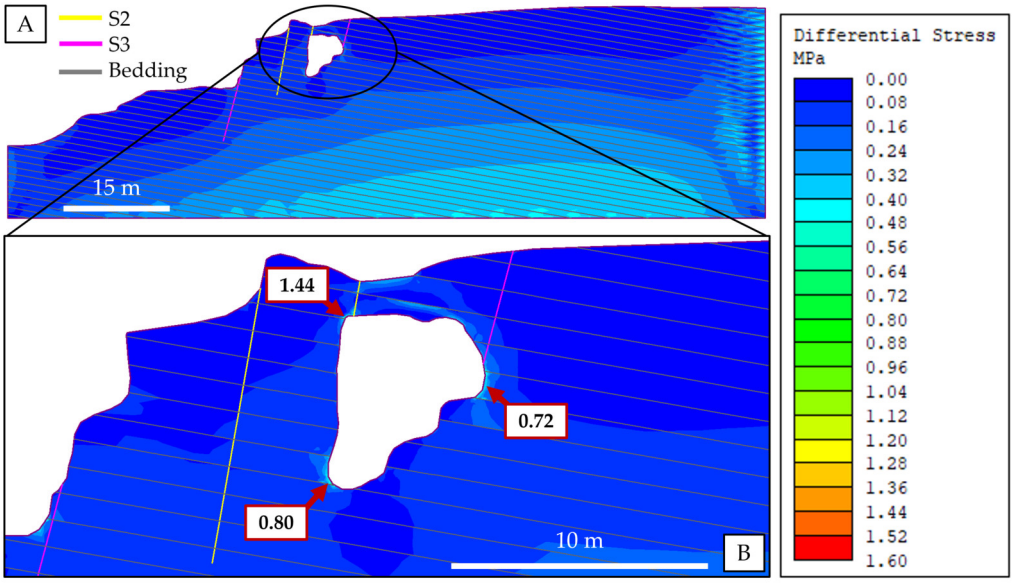

Figure 3.21: Differential stresses resulting from geotechnical modelling along the CC' cross-section (A). Detail of the obtained differential stress values (B).

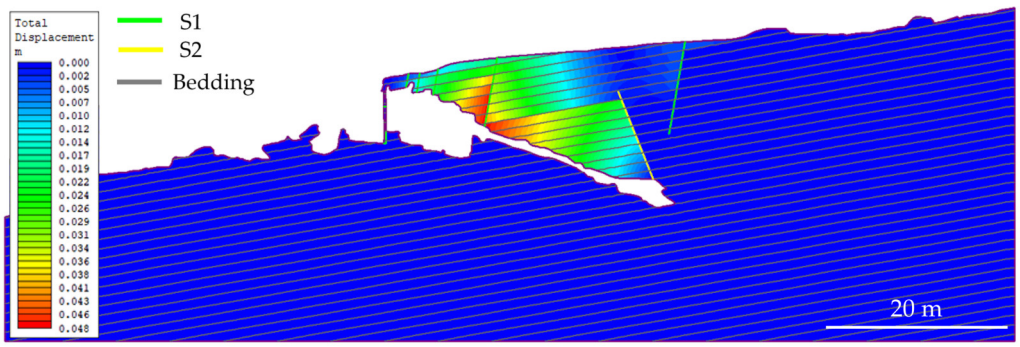

Figure 3.22: Displacement values resulting from geotechnical modelling along cross-section AA'.

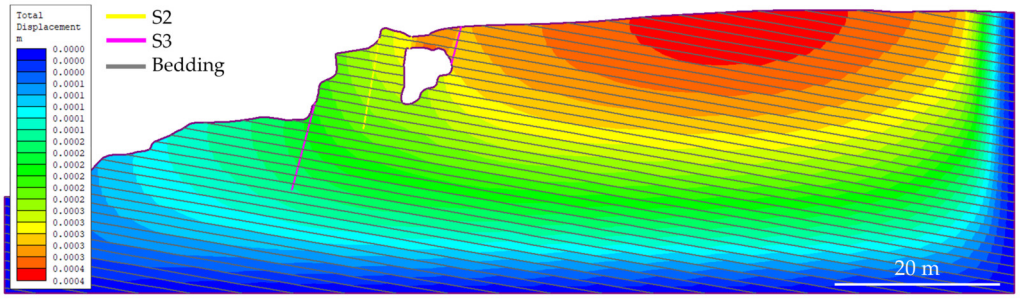

Figure 3.23: Displacement values resulting from geotechnical modelling along cross-section CC'.

3.1.7 Discussion

The integration of several geomatic techniques, combined with data from a traditional engineering–geological survey, has produced a large set of results essential for the geological characterization of the site and the identification of hazardous slope conditions. The joint use of UAV photogrammetry and SLAM-based laser scanning proved to be particularly effective in ensuring both accuracy and completeness. Earlier studies have highlighted how terrestrial LiDAR is reliable but time-consuming in terms of acquisition and processing (**Basantes et al., 2017**; **Buchroithner & Gaisecker, 2009**; **Büyüksalih et al., 2020**; **Cosso et al., 2014**; **Gallay et al., 2015**; **González-Aguilera et al., 2009**; **Grussenmeyer et al., 2012**; **Lerma et al., 2010**; **Nocerino et al., 2019**; **Rüther et al., 2009**; **Salvini et al., 2014**; **Shults et al., 2019**; **Zlot & Bosse, 2014**). With the development

of SLAM systems—operable manually or integrated on UAVs and ground robots—laser scanning has improved further in terms of acquisition speed, density of captured points, and completeness (**La Scalea et al., 2019**; **Petracek et al., 2021**; **Blank et al., 2021**; **Giordan et al., 2021**; **Grasso et al., 2023**).

In this case study, UAVs and robotic systems could not be employed inside the cave due to the narrow and tortuous morphology and the presence of speleothems. Portable SLAM-based LiDAR, instead, enabled the complete mapping of the four chambers with optimal resolution and spatial accuracy, also thanks to a rigorous topographic survey, and in less than one hour of acquisition. The low RMSE values obtained confirm the successful alignment and georeferencing of the dense 3D point clouds generated from UAV photogrammetry and laser scanning. The resulting merged global model proved to be a fundamental tool, not only to map visible joints, both internal and external, but also to assess their persistence. This aspect represents a key outcome of the present work, since the moderate thickness of the cave vault made it possible to model discontinuity lengths with accuracy and, consequently, perform reliable numerical analyses.

Engineering–geological characterization indicates that the rock mass is of generally good quality, though stability issues may arise on slopes steeper than 60°. These slopes, when intersected by unfavorable discontinuities, can lead to block and wedge failures or toppling mechanisms. Such conditions are consistent with field observations, where relict sliding planes and rockfall deposits were identified at the foot of the cliffs. Given that empirical classification methods are inherently limited, they were complemented by kinematic stability analyses performed on three representative slopes. Results highlighted wedge sliding and direct/oblique toppling as the dominant mechanisms, whereas planar sliding appeared possible only on slope V3, which shows the most critical geometrical relationships. In particular, wedge sliding was found to occur mainly through S1–S2 and S1–S3 intersections, while direct and oblique toppling did not reveal a predominant combination. Overall, the slopes surrounding Grotta Paglicci are prone to kinematic insta-

bilities, thus justifying the implementation of deterministic dynamic analyses to identify the most vulnerable areas.

The dynamic stability analysis of blocks n.1 and n.2 highlights a marked contrast between their apparent stability under standard conditions and their rapid transition to criticality when external factors are introduced. For Block n.1, the flexural toppling mechanism shows FoS values of 6.74 under static conditions and 4.59 with seismic input, suggesting overall stability. However, when joint water filling is considered, FoS decreases drastically, reaching 2.74 at 67% saturation and falling below 1 with only 1% additional filling. A similar pattern emerges under combined seismic and water-loading conditions, where FoS drops from 2.97 at 52% to instability at 53%.

Block n.2 exhibits comparable behaviour: both the direct/oblique toppling (2a) and flexural toppling (2b) cases record FoS values above 10 under static conditions (10.88 and 10.81, respectively) yet lose stability abruptly once joint filling exceeds 68–69% (DT/OT) or 66–67% (FT). Under the combined effect of seismic loading and water, instability is reached already at 55–56% and 53–54% saturation.

These results underline that, although the blocks appear secure in dry conditions, they are extremely sensitive to hydrogeological changes, with even minimal increments in water pressure leading to instability. The additional RocPlane analysis for Block n.1 confirms this fragility: planar sliding along slope V2 shows FoS values of only 0.80 under standard conditions and 0.62 with seismic input. This dual evidence suggests that the main hazard factor is not the seismic load itself, but its interaction with water infiltration in the discontinuities.

Numerical modelling offered a more detailed assessment of both the cave and the external rock walls, providing insights into potential collapse scenarios and conservation strategies. Comparable applications in other hypogeal contexts confirm the usefulness of 2D numerical modelling for stability assessment and the design of preventive interventions (**Geniş & Çolak, 2015**; **Rodríguez et al., 2023**). In this study, numerical simulations en-

abled the identification of critical stress zones that may evolve into instabilities. According to the method proposed by **Salvini et al. (2022)**, the threshold differential stress for failure in slightly fractured rock masses can be estimated. For the "Monte Calvo del Gargano" limestone, with an average UCS of 37 MPa (**Italferr, 2015**), the critical differential stress is about 12.12 MPa, according to Equation (3.1), proposed by **Hoek & Brown, 1980** and **Martin et al., 1999**:

$$\sigma_1 - \sigma_3 \geq 0.33 \cdot 37\,\text{MPa} = 12.21\,\text{MPa} \tag{3.1}$$

Results show that, while most cross-sections present values well below this threshold (<3 MPa), the Atrium section recorded peaks up to 39 MPa (Figure 3.19).

Based on **Cosgrove (1998)**, if the differential stress is below four times the tensile strength, extensional failure may occur. In contrast, when differential stress exceeds four times the tensile strength of the rock, shear failure is likely to develop.

Laboratory investigations on intact samples of calcareous rocks indicate that their tensile strength typically ranges between 1 and 10 MPa, with an average value close to 5 ± 2 MPa (**Farmer, 1968**; **Hardy & Jayaraman, 1970**; **Ippolito et al., 1975**; **Miller, 1965**; **Paronuzzi & Serafini, 2008**; **Szechy, 1966**).

Following the approach proposed by **Cosgrove (1998)**, a threshold of 28 MPa can be used to distinguish between different failure mechanisms.

Referring to the value of 12.12 MPa obtained in Equation (3.1), it follows that shear failure may occur when $\sigma_1 - \sigma_3 > 28\,\text{MPa}$, whereas extensional failure is expected for $\sigma_1 - \sigma_3 < 28\,\text{MPa}$.

The analysis in Figure 3.19 highlights certain areas where shear failures could potentially develop, although they have not yet been observed, likely because of the presence of unknown rock bridges along the discontinuities.

In contrast, Figures 3.20 and 3.21 show only extensional failure mechanisms, which

are considered to have a low likelihood of occurrence due to the very limited differential stress values involved.

Nevertheless, the elevated stress values observed in Figure 3.19 are not corroborated by Figures 3.20 and 3.21, where the cross-sections were constructed approximately orthogonal to AA'. In particular, the high stresses identified along the AA' profile, reaching 39 MPa near the cave entrance (Figure 3.19), are likely attributable to the limited thickness of the left lateral wall of the Atrium dome, which appears insufficient to adequately redistribute the load induced by the overlying roof material (**Oreste et al., 2023**; **Sakellariou et al., 2020**). This interpretation could be validated by calibrating the numerical model by in situ stress measurements, as suggested in **Salvini et al. (2022)**.

The assessment of displacements along the different cross-sections highlighted potential instabilities in the transition area between the Atrium and Chamber 1. In particular, the analysis of section AA' revealed that instability phenomena could develop due to the interaction between the S1 joint set, the bedding planes, and the cave roof (Figure 3.22). This finding is further supported by the kinematic stability analysis, which indicates that planar sliding may occur at the intersection of the S1 joint system with slope V3. The scenario fulfills both conditions necessary for planar sliding to take place, namely the daylighting of the joint on the slope surface and a dip angle greater than the friction angle (**Markland, 1972**).

Based on these results, and considering the type of failure mechanisms likely to develop, it was possible to delineate areas where protective measures are required to mitigate risks for personnel engaged in archaeological, anthropological, geological, and maintenance activities. A dedicated project concerning such safety interventions has already been submitted to the competent authorities, in line with the technical recommendations derived from this study. In particular, the cross-sections obtained from topographic surveys and 3D modelling were used to estimate the thickness of the vertical wall, allowing the definition of the maximum anchorage depth for threaded rods to be installed on the

external multi-step slope. Moreover, the integration of engineering–geological data with the kinematic analysis identified zones affected by hazardous instabilities where the only viable option is the removal (scaling) of unstable rock masses. Complementary to these measures, the installation of an in situ monitoring system has been planned, powered by solar energy, and equipped with electrical crackmeters and inclinometers connected to real-time remote alert systems.

3.1.8 Conclusions

In the rapidly advancing domain of geospatial data acquisition and 3D modelling, the growing demand for precision, efficiency, and adaptability in mapping has fostered the adoption of multi-technique survey strategies. The approach employed in this study combines the complementary strengths of UAV photogrammetry and SLAM-based LiDAR mapping. Each technique offers distinct advantages, and their integration provides a versatile framework capable of addressing the diverse challenges of surveying in complex environments. This combination not only ensures high accuracy and detail but also streamlines field operations, reducing both time and costs.

At Grotta Paglicci, the application of this integrated geomatic approach has yielded a detailed understanding of the cave's morphology, supplying essential datasets for comprehensive engineering–geological characterization. The synergy of internal and external 3D point clouds has delivered a holistic perspective on the cave system, overcoming restrictions imposed by narrow passages and speleothem formations, while also enabling the assessment of joint persistence and slope stability.

The relevance of this work lies in its ability to merge innovative digital tools with consolidated geological practices. The resulting stability assessment not only illustrates the current condition of the cave but also provides a foundation for future conservation strategies. Moreover, the methodology presented here is adaptable: it can be applied

to static or multitemporal surveys, and extended to large artificial underground cavities, while ensuring an effective balance between survey accuracy, data processing demands, and the monitoring of stress and displacement.

Ultimately, this study demonstrates the potential of integrating advanced geomatic techniques with traditional approaches. By offering new insights into the geological complexities of Grotta Paglicci, it also establishes a replicable framework for sustainable management and preservation of archaeological and natural heritage sites.

3.2 Multitemporal slope stability analysis of the Sabereebi rock-cut Monastic Complex (Georgia)

3.2.1 Introduction

Rock-cut cultural heritage sites represent unique and irreplaceable testimonies of human interaction with the geological environment. Among these, the Sabereebi Monastery Complex, carved into a sedimentary succession cliff in southern Georgia, is one of the most significant rupestrian landmarks in the Caucasus.

Carved between the 6^{th} and 13^{th} centuries into a stratified cliff face composed of weak sedimentary rocks—including sandstone, siltstone, conglomerate, and clay—the complex comprises five main caves and numerous sub-caves, which host chapels, monastic cells, and wall paintings. Today, Sabereebi represents a fragile yet emblematic example of medieval Georgian ecclesiastical architecture, uniquely embedded within an actively evolving geomorphological setting.

However, such rock-cut structures are particularly vulnerable to both natural and anthropogenic degradation processes, including weathering, erosion, and seismic activity. Located on the tectono-erosive ridges of the Iori Upland, the monastery lies within an arid steppe environment marked by pronounced thermal excursions (reaching 60 °C), persistent strong winds, and rare yet intense precipitation events (**Gagua & Mumladze 2012**; **Kordzakhia 1964**; **Mumladze & Lomidze 2012**; **Tielidze et al. 2019a**, **2019b**). These environmental and geological conditions significantly influence the mechanical behavior and progressive instability of the rock.

Understanding the formation, evolution, and current stability of these sites is therefore essential for their long-term conservation and sustainable management. Comparable challenges are observed in other notable rupestrian contexts such as Vardzia in southern

Georgia, the cave monasteries of Cappadocia in Turkey, and the sandstone façades of Petra in Jordan—many of which are included in the UNESCO World Heritage List or Tentative List (**Frodella et al., 2021**). These examples, excavated in weak lithologies and subject to harsh climatic and seismic conditions, highlight the global urgency of integrating geoscientific approaches within heritage preservation frameworks (**Frodella et al., 2021**).

In recent years, several studies have investigated the structural stability of the Sabereebi Complex using advanced 3D modeling and monitoring techniques. Notably, high-resolution FEM modelling has been employed to assess stress distribution within the rock mass (**Domej et al., 2022**), while broader regional research has explored instability scenarios in similar cultural landscapes, such as David Gareja (**Margottini et al., 2020**), and emphasized the value of close-range non-destructive techniques for site-specific conservation planning (**Frodella et al., 2021**). Recent academic work conducted at the University of Florence (Italy) has underlined the role of systematic monitoring in mitigating landslide-related risks in Georgian rupestrian sites (**Frullini, 2022**).

Despite these advances, there remains a lack of long-term, comparative spatial analyses based on multitemporal datasets capable of quantifying progressive degradation trends and identifying potential detachment zones within the Sabereebi cliffs. The present study addresses this gap by analyzing TLS and drone-based photogrammetric data collected in 2018 and 2025, enabling a detailed three-dimensional assessment of morphological changes over time.

By integrating geospatial technologies with field-based geological observations, this research furnishes new insights into the degradation dynamics affecting the Sabereebi Monastery Complex. The results aim to support both the scientific understanding of slope instability in soft-rock environments and practical conservation and risk-mitigation strategies in fragile rupestrian landscapes.

3.2.2 Archeological framework

The Sabereebi Monastic Complex, carved into the soft volcanic rocks of the Gareja semi-desert in southeastern Georgia, represents an outstanding example of medieval Georgian rupestrian architecture. The complex includes a series of small rock-hewn churches, chapels, and monastic cells, primarily dated to the 9th–11th centuries CE (**Volskaja, 1983**; **Skhirtladze, 1985**).

Architecturally, the ensemble demonstrates a deliberate adaptation to the local geomorphology, which is directly linked to the site's current stability and conservation challenges. As part of the broader Davit Gareja monastic system, Sabereebi shares typological features and historical significance with nearby complexes such as Lavra and Natlismtsemeli (**Margottini et al., 2020**; **Gaprindashvili, 1987**). Although systematic archaeological excavations have not yet been undertaken at Sabereebi, exploratory investigations since the 1970s, particularly by Gaprindashvili and Tvalchrelidze, revealed important artefacts and burials, including a bronze ring and fragments of monastic garments discovered near the southern entrance of one of the cave churches. These finds confirm the complex's use as an active monastic center during the early medieval period and suggest the presence of a sophisticated liturgical and commemorative landscape.

The site is also notable for its mural paintings, which survive in varying states of preservation and reflect a transitional stage in the development of Georgian monumental art. According to **Skhirtladze (1997)**, the Sabereebi frescoes exhibit a structured yet restrained decorative program focused on essential iconographic elements such as Theophanies, Crucifixions, and depictions of Warrior Saints. The murals are mainly located in apses and along the north walls, whereas later phases reveal greater architectural integration and the use of ornamental details.

Two of the internal churches, the south-easternmost and the one just on the left side of it, are particularly significant, displaying complex compositions organized in multiple

registers and domes adorned with relief crosses or stellar motifs—features consistent with developments in other major Georgian mural cycles (**Volskaja, 1983**; **Skhirtladze, 1985**; **Ševjakova, 1983**).

Given the host rock's fragile lithology and the architectural integration of the complex within an erosive cliff system, both the mural ensemble and the site's archaeological integrity remain at elevated risk. This condition highlights the urgent need for detailed geomechanical analyses and site-specific conservation strategies (**Domej et al., 2022**; **Frodella et al., 2021**; **Frullini, 2022**).

3.2.3 Geological and geomorphological settings

The Sabereebi Monastery Complex is located within the Kura Transcaucasian intermontane basin. This region is characterized by highly deformed Oligocene–Miocene sedimentary formations that overlie the eastern sector of the Adjara–Trialeti fold-and-thrust belt (Figure 3.24, **Gusmeo et al., 2021**).

The broader structural framework (Figure 3.24) shows the main tectonic units and fault systems of the Eastern Anatolia–Caucasus region, where compressional and strike-slip structures are associated with the Arabia–Eurasia collision zone (**Cavazza et al., 2019**; **Sosson et al., 2010**).

Locally, the site exhibits a typical monocline "hogback-type" ridge, with strata gently dipping northeastwards (Figure 3.25). These northwest–southeast-trending ridges are representative of the Iori Upland, an intermountain plateau within the Iveria Plain that rises to approximately 1000 m a.s.l. from the depression between the Greater and Lesser Caucasus. The Iori Upland displays a hilly morphology composed of anticlinal and synclinal hummocks of tectono-erosive origin, with relative heights reaching up to 300 m above the surrounding lowlands and extending for several kilometres (**Javakhishvili et al., 2019**; **Tielidze et al., 2019a, 2019c**).

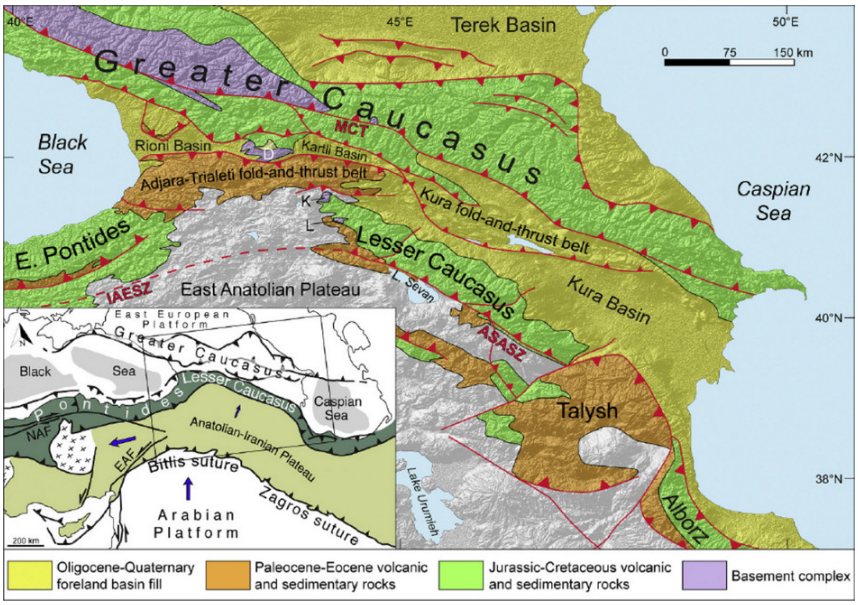

Figure 3.24: Main tectonic units and structures of the Eastern Anatolia-Caucasian region superimposed on an ASTER GDEM shaded relief map (from **Gusmeo et al., 2021**). ASASZ = Amasia-Sevan-Akera suture zone; D = Dzirula Massif; IAESZ = Izmir-Ankara-Erzinçan suture zone; K = Khrami Massif; L = Loki Massif; MCT = Main Caucasian Thrust. Red lines with triangles indicate thrusts; red lines are normal, strike-slip or unknown kinematics faults. Inset: Tectonic sketch map of the Arabia-Eurasia collision zone modified after **Cavazza et al. (2019)** and **Sosson et al. (2010)**. EAF = Eastern Anatolian Fault; NAF = Northern Anatolian Fault.

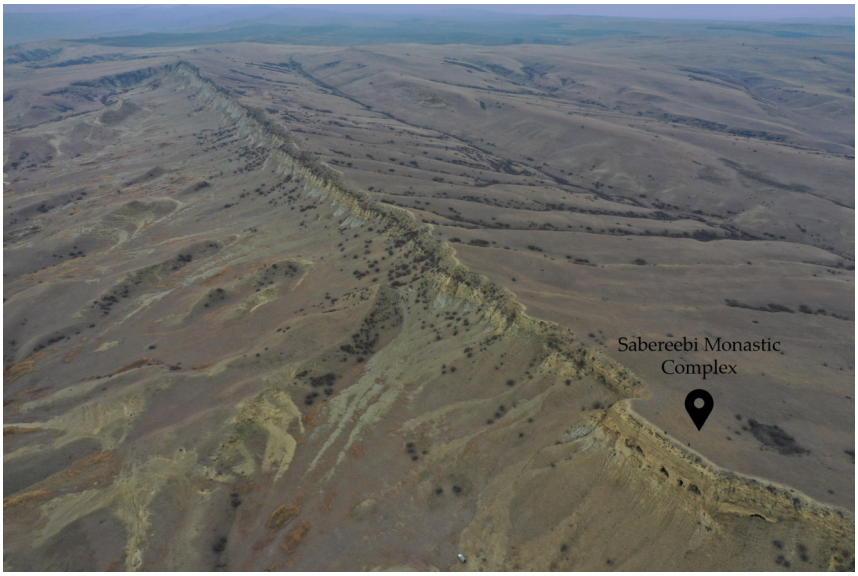

Figure 3.25: Example of cuesta-type northwest–southeast-trending ridges of the Iori Upland.

The general basin morphologies of the region are asymmetric due to reverse faulting. Ridges typically display low-gradient, northeast-facing slopes and nearly vertical cliffs on their southwest sides, which gradually evolve into gentler slopes at the cliff base. These basal zones are often dissected by minor drainage channels that serve as conduits for earth and debris flows, accelerating erosion. Ridge concavities predisposed to channel incision are frequently conditioned by drainage networks developed on the opposite flanks, demonstrating the strong coupling between structural and surface processes in the area.

The lithostratigraphic succession of the Sabereebi area is mainly composed by soft sedimentary rocks ranging in age from the Lower Miocene to the Pliocene, locally overlain by Quaternary deposits (**Gamkrelidze, 1992**; **Gobejishvili & Tsereteli, 2012**; **Tielidze et al., 2019a**; **Tsereteli, 1964**).

The Lower Miocene sequence consists of sandy clays and massive clays interbedded with sands and conglomerates.

The Upper Miocene deposits comprise shallow-marine to coastal facies with calcareous sandstones, sandy clays, and continental mottled clays, locally containing thin volcanic-ash and conglomerate levels.

Pliocene to Upper Pliocene deposits, belonging to the Aghchagil Stage (indicated as N_2^3aK in Figure 3.26), are represented by coarse-grained sandstones with small pebbles and basal conglomerates interlayered with volcanic ash, indicating alternating continental and marine conditions. Quaternary alluvial, diluvial, and proluvial covers are widespread within valley floors and depressions (Figure 3.26).

A detailed geological cross-section of the Sabereebi cliff (Figure 3.27) highlights a sedimentary sequence associated with a marine depositional cycle (**Margottini & Spizzichino, 2021**). From top to bottom, six main units can be identified: (i) a high-permeability heterogeneous topsoil composed of clay, silt, sand, and gravel in varying proportions; (ii) a weathered and highly fractured siltstone; (iii) a natural marine conglomerate with fine, rounded clasts; (iv) a weakly cemented and fractured sandstone; (v) a second weathered

siltstone horizon; and (vi) a clayey bedrock deposit forming the basal layer.

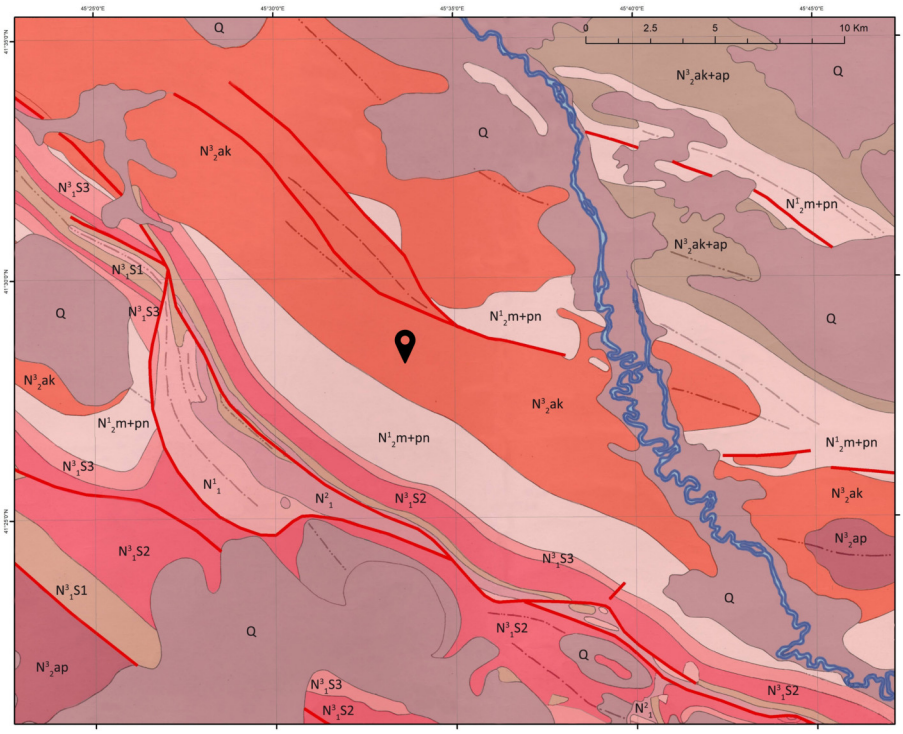

Figure 3.26: Geological Map of the Basin of the Middle Reaches of the Kura River by D. Papava, 1976, scale 1 : 100 000. Stamped: Geological Survey Bureau, State company "Gruzneft", GEOLFOND D1283. **Q** = Quaternary continental unconsolidated alluvial, colluvial, and eluvial deposits. N_2^3**ap** = Apsheronian (Lower Pliocene), continental and marine molasse composed of sands, loams, clays, and sandstones. N_2^3**ak+ap** = Apsheronian–Akchagylian transitional facies, continental and marine molasse including conglomerates, sandstones, clays, loams, and volcanic tuff intercalations. N_2^3**ak** = Akchagylian (Upper Pliocene), continental and marine molasse consisting of conglomerates, sandstones, sands, clays, and volcanic ash intercalations. N_2^1**m+pn** = Meotian and Pontian (Upper Miocene), marine and continental molasse including conglomerates, sandstones, and clays. N_1^3**S1–S3** = Sarmatian (Upper Miocene), marine to continental molasse composed of clays, sandstones, conglomerates, marls, and limestones. N_1^2 = Middle Miocene marine molasse consisting of clays, sandstones, conglomerates (locally with basal conglomerates), marls, oolitic and arenaceous limestones. N_1^1 = Maikop Series (Lower Miocene), marine molasse comprising sandstones, gritstones, weakly carbonaceous clays with marl intercalations, and locally gypsiferous clays and sandstones. **Structural elements**: undifferentiated faults are represented as simple red lines. **Fold axes**: anticline axes are shown with dot–dash lines, whereas syncline axes are represented with dot–dot–dash lines. The black pin marks the location of the Sabereebi Monastery Complex.

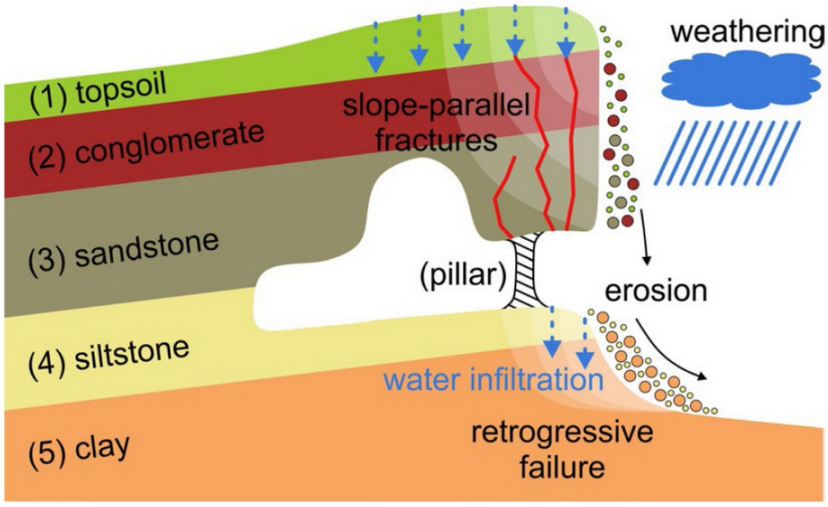

Figure 3.27: Geology of Sabereebi (from **Domej et al., 2022**)

Cuesta-type ridges dominate the area's morphology and correspond to the more sandstone-rich portions of the sedimentary sequence. These alternate with relatively flat highlands and badland morphologies, where fine-grained, silty-clayey layers are exposed. The combination of contrasting permeability and mechanical resistance among layers drives differential erosion, producing the characteristic stepped slopes of the Iori Upland.

The Sabereebi caves were excavated precisely along these lithological transitions, where resistant sandstone beds overlie weaker clayey strata. Progressive weathering and undercutting at these interfaces promote local retreat and the formation of overhangs, which directly influence the evolution and preservation of the monastic structures (**Gobejishvili & Tielidze, 2019**; **Margottini et al., 2019**).

From a geotechnical perspective, the principal concern at Sabereebi lies in the friable and fissured nature of the host rocks. The upper units consist of porous siltstone and conglomerate with low density and high permeability, while the lower layers are mainly composed by clay. This lithological contrast facilitates infiltration and water accumulation, accelerating mechanical weakening and chemical weathering (**Margottini & Spizzichino,**

2021).

Water percolation along discontinuities promotes erosion and retrogressive failures, particularly within the clay-rich basal levels. Such processes endanger not only the slope stability but also the integrity of the carved elements—pillars, walls, and ceilings—within the monastic chambers. The plasticity and low cohesion of the clayey layer increase the likelihood of sliding or collapse, especially following intense rainfall events or seismic shaking.

Geotechnical laboratory analyses of representative samples documented by **Frodella et al. (2021)** confirm the low mechanical strength of the host rock and emphasize the rock mass's critical fragility, which, combined with climatic and tectonic stresses, results in frequent minor rockfalls, surface spalling, and material loss. Such processes threaten both the natural stability of the slope and the conservation of invaluable rupestrian heritage, including fresco-decorated chapels, cross-dome churches, galleries, and refectories carved within the cliff.

3.2.4 Materials and Methods

To evaluate the instability processes affecting the Sabereebi Monastic Complex, this study applied an integrated approach combining remote sensing, structural analysis, and numerical modeling. High-resolution 3D datasets from two survey campaigns (years 2018 and 2025), including TLS and UAV photogrammetric acquisitions, were processed to generate dense point clouds and DEMs. Morphological changes between the two epochs were assessed using the M3C2 algorithm (*Multiscale Model-to-Model Cloud Comparison*) in CloudCompare (**CloudCompare, 2021**), enabling the identification of erosion patterns, block detachment areas, and other degradation features. These data were incorporated into a 3D FEM model developed in Rocscience™ RS3 (Version 4.039; **Rocscience™ Inc. 2025**) to analyze slope stability and potential failure mechanisms. Overall, the

multi-sensor workflow provides a robust foundation for characterizing and mitigating the geohazards threatening this rock-cut heritage site.

3.2.4.1 Previous data

3.2.4.1.1 UAV and Terrestrial Laser Scanning surveys

The first dataset, corresponding to the 2018 survey, consists exclusively of terrestrial laser scanning data acquired during a field campaign conducted by the University of Milano–Bicocca (Italy). Data were collected using a RIEGL^{TM} VZ-1000 V-Line terrestrial laser scanner from three scan positions strategically placed on the left, central, and right sectors of the site's bottom area to ensure full coverage of the cliff and the rock-cut structures. The three acquisitions were subsequently merged to obtain a single point cloud representing the overall morphology of the Sabereebi complex. The 2018 points cloud contains approximately 127 million points (with spatial resolution varying from millimetric to centimetric in rock chambers), in local coordinates, providing a detailed three-dimensional description of the main architectural and geomorphological features. The point cloud has only information related to coordinates and intensity (no RGB data are present).

3.2.4.1.2 Geotechnical parameters for FEM simulation

The geotechnical parameters used in the FEM stability analyses to simulate the mechanical behavior of the lithological units that form the Sabereebi cliff, have been identified from laboratory analyses described in Frodella et al. (2021) and from literature (**Bergamini, 2020**; **Domej et al., 2022**; **Gasbarrone, 2005**; **Margottini & Spizzichino, 2020**; **Shafiei & Dusseault, 2008**). The notations "μ" and "e", shown in Table 3.17, indicate the mean and the estimated values, respectively.

An elasto-plastic Mohr–Coulomb constitutive behavior (**Coulomb, 1776**) was adopted

for all materials; it is characterized by six principal parameters: Young's modulus (E), Poisson's ratio (ν), unit weight (γ), friction angle (ϕ), cohesion (c), and dilatancy angle (ψ) whose values are shown in Table 3.17.

Table 3.17: Geotechnical parameters of lithologies present in the Sabereebi Cave Monastery area (modified from **Domej et al., 2022**).

Layer	E **[MPa]**	ν **[–]**	γ **[kN/m^3]**	ϕ [°]	c **[kPa]**	ψ [°]
Topsoil	1.1	0.3	18.0	21.5	25	8.5
Conglomerate	5000	0.3	20.4	31.5	3500	8.5
Sandstone	155μ	$0.2e$	16.5μ	42.0	150	$3e$
Siltstone	285μ	$0.2e$	15.8μ	42.0	150	$3e$
Clay	125	0.3	19.2	20.5	20	8.5

3.2.4.2 New data

3.2.4.2.1 Terrestrial laser scanning

To capture high-resolution 3D data for rockfall modeling and slope stability analysis, a Trimble^{TM} TX8 TLS was utilized for the year 2025 University of Siena survey. In total, eighteen scans were conducted at a spatial resolution of 22.6 mm at 30 m, producing a high-density point cloud ideal for close-range analysis where detailed topographic documentation is essential for understanding potential rockfall initiation zones and their interaction with surrounding features. Each scan contained approximately 30 million points.

To ensure full coverage of the upper cliff face and mitigate occlusions that could not be resolved from close-range positions, two additional long-range scans were acquired from the valley floor at about 200 m. Although these scans have a coarser nominal resolution (75.4 mm at 300 m), they were essential for capturing the overall geometry of the upper limestone wall and integrating missing sections that were not visible from the closer stations due to overhangs and topographic shadow zones. In this case, each scan collected roughly 110 million points, yielding a comprehensive 3D representation of the slope.

The combination of the twenty scans allowed us to produce a detailed, wide-ranging dataset that encompassed both the fine-scale morphology of the caves and the large-scale slope geometry, with a total number of 738 million points. The acquired data was subsequently processed and registered using the Iterative Closest Point (ICP) algorithm in Trimble™ Realworks software. Manual refinement was subsequently performed to correct minor residual misalignments, particularly in complex sectors such as cave entrances and vertical cliff faces. Subsequently, the point cloud was resampled to produce a coherent point cloud referenced to the WGS84/UTM Zone 38N coordinate system.

3.2.4.2.2 Unmanned aerial vehicle survey

To complement the TLS dataset, a new UAV survey was conducted using a DJI™ Mavic 2 Pro UAV equipped with an RGB Hasselblad® L1D-20C camera. The camera's 10.26 mm lens ensured sharp, precise imagery, ideal for documenting fine-scale morphological features such as rockfall scars and slope discontinuities.

The campaign focused on capturing high-resolution imagery of the study area, particularly the cave sectors and adjacent slopes that were inaccessible with terrestrial methods. Data acquisition was performed both manually and automatically, with the drone capturing both nadiral (vertical) and oblique (frontal) images to ensure comprehensive coverage of topographic features from multiple perspectives. This approach facilitated a more detailed reconstruction of the surface geometry and improved the overall accuracy of the 3D model. The UAV flight plan was designed to optimize image overlap and guarantee sufficient ground control for accurate georeferencing.

Image processing was carried out in Agisoft™ Metashape Professional software (Version 2.0.2; **Agisoft LLC, 2023**), which employs Structure-from-Motion (SfM) and Multi-View Stereo (MVS) algorithms to generate high-quality 3D models from overlapping photographs.

To achieve accurate georeferencing, Ground Control Points (GCPs) were sited using

planar black-and-white square targets (20 cm edge length) distributed across the slope and on the external cave walls. GCPs were imported into the photogrammetric workflow to optimize the photo bundle adjustment, minimize geometric distortions, and improve absolute positional accuracy. Their coordinates were measured with a high precision GNSS receiver (Stonex^{TM} S9III Plus) operating in Network Real-Time Kinematic (NRTK) mode.

The resulting photogrammetric model was used to create an updated 3D point cloud and to supplement the TLS dataset, providing additional insights into the cave and slope morphology and improving the spatial resolution of the overall topographic model. The integration of UAV-derived and TLS data facilitated a comprehensive 3D representation of the study area, combining fine-scale and large-scale information essential for the subsequent FEM stability analysis. Characteristics and spatial resolution of the year 2025 outputs are described in the section dedicated to the results of the study.

3.2.4.3 Structural discontinuity mapping

To characterize the structural setting of the Sabereebi Monastic Complex and assess the influence of discontinuities on slope instability, a digital fracture-mapping activity was conducted using the Feature Set tool in the Trimble^{TM} Scan Explorer environment. The analysis was based on the high-resolution, colorized TLS 3D point cloud of the year 2025, which provided detailed surface geometry and visual context for structural interpretation. Discontinuities were mapped both on the external slope surface and within the inner cave chambers, with particular attention to joints intersecting carved walls, ceilings, and natural overhangs. Each mapped discontinuity was recorded in an `*.ASCII` file containing spatial coordinates in the WGS84/UTM Zone 38N coordinate system (EPSG:32638). These files were exported and, subsequently, imported into CloudCompare software to be visualized and analyzed. Orientation data, including dip and dip direction of each single discontinuity, was measured and cross-checked against the 3D point cloud to ensure geometric accuracy

and completeness. In addition to the fractures identified within the TLS-derived dataset, several discontinuities were manually digitized on the UAV-based photogrammetric model by examining high-resolution imagery (Figure 3.28). This integration allowed for the recognition of joint traces that were not clearly visible in the TLS data, particularly along steep cliff sections and overhanging surfaces where terrestrial scanning coverage was limited.

The spatially referenced nature of the mapped features enabled precise correlation with slope morphology and mesh geometries, supporting the identification of structurally controlled failure mechanisms relevant to the site's geomechanical stability.

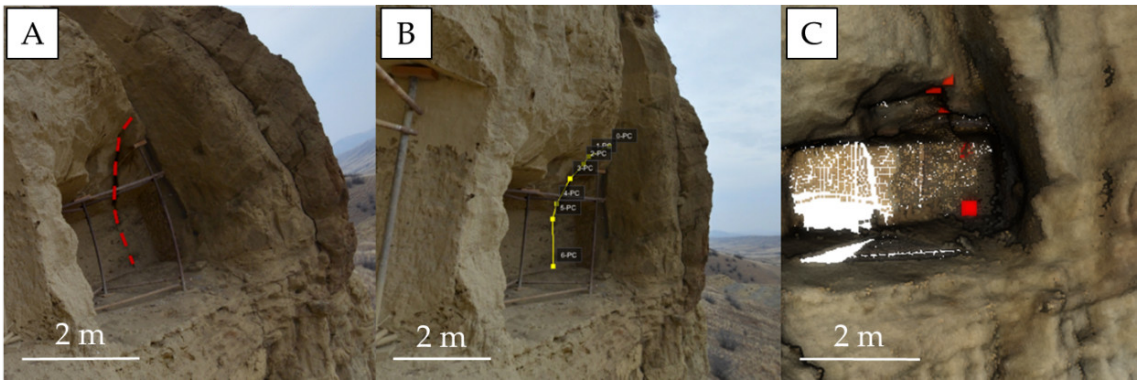

Figure 3.28: Example of discontinuity extraction: panel (A) shows the visual definition on image; panel (B) shows the sampling on image in Trimble™ Scan Explorer with point cloud as base data for extraction; panel (C) shows, in CloudCompare environment, the georeferenced points, in red, coming from the `*.ASCII` file

3.2.4.4 Multitemporal point cloud comparison

To assess morphological changes and surface degradation at the Sabereebi Monastic Complex over time, a multitemporal comparison of the 3D point clouds acquired in 2018 and 2025 was performed. The analysis employed the M3C2 algorithm implemented in CloudCompare.

Prior to change detection, all point clouds were co-registered in Trimble™ RealWorks using a cloud-based registration workflow. This method bases on global surface matching

rather than local feature alignment and permits to achieve a precise alignment represented by a Root Mean Square Error (RMSE) later adopted as input parameter for the registration uncertainty in the M3C2 computation.

The M3C2 algorithm was used to compute signed distances between multitemporal point clouds, following the direct point-to-point method introduced by **Lague et al. (2013)**. For each core point, a local normal vector was estimated using a neighborhood of diameter D (normal scale). A cylindrical neighborhood of diameter d (projection scale) and defined depth were then used to compute the distance between the mean positions of the two clouds along the normal direction, allowing 3D change detection without requiring any meshing or gridding. For every measured distance, the algorithm also evaluates the Level Of Detection at 95% confidence (LOD95%), which accounts for the combined influence of surface roughness and coregistration error. Following **Lague et al. (2013)**, the LOD95% is computed as:

$$\mathrm{LOD}_{95\%} = 1.96 \times \left(\sqrt{\frac{s_1(d)^2}{n_1} + \frac{s_2(d)^2}{n_2}} + \mathrm{coreg}\right) \tag{3.2}$$

where $s_1(d)^2$ and $s_2(d)^2$ represent the local roughness of the two point clouds within the projection scale d, n_1 and n_2 are the number of points contained in the cylindrical neighborhoods, and coreg is the coregistration error between the multitemporal data. A change is considered statistically significant only when its magnitude exceeds the computed LOD95%. To quantify the volume of detached material within areas exhibiting statistically significant retreat, the affected point-cloud portions were isolated, merged, and prepared for surface reconstruction. Three-dimensional meshes were generated using the *Poisson Surface Reconstruction* algorithm implemented in CloudCompare, following the method introduced by **Kazhdan et al. (2006)**. This algorithm reconstructs a continuous and topologically closed surface starting from point clouds with oriented normals. The method interprets the normals as samples of a vector field defined over the underlying surface and

solves a Poisson equation whose solution yields a smooth implicit function. The target surface is then extracted as the zero-level set of this function. In practice, this approach integrates the observed normals into a coherent global surface representation, making the resulting mesh robust to noise, small gaps, and irregular point spacing.

The meshes produced via *Poisson Surface Reconstruction* algorithm are particularly suitable for geomorphological and geotechnical applications, as they provide continuous, regular geometries that facilitate accurate volumetric computations. Final volume estimates were obtained using the *Measure Volume* tool within CloudCompare, applied to the reconstructed mesh models.

3.2.4.5 FEM slope stability analysis

To assess the slope stability conditions at the Sabereebi Monastic Complex, a three-dimensional FEM model was created using Rocscience^{TM} RS3 (Version 4.039; **Rocscience^{TM} Inc. 2025**). High-resolution topographic data obtained through TLS and UAV-based photogrammetry were integrated and processed in Agisoft^{TM} Metashape to generate dense point clouds and surface meshes. After cleaning and simplification, the 3D geometry of the cliff was exported in a RS3-compatible format (`*.obj`). The imported surface model was discretized using a uniform 4-noded tetrahedral mesh (number of nodes equal to 646,621 and number of tetrahedra equals to 3,667,972), and boundary conditions were assigned using the *Auto Restrain (Surface)* option in RS3, which automatically applies standard default restraints to surface-based models. With this configuration, fixed XYZ displacement constraints were assigned to the bottom and lateral boundaries of the model domain in such a way to prevent any rigid-body translation or rotation of the external boundary. The upper surface, corresponding to the natural ground surface, was left completely unconstrained (free surface).

The geological framework, and its geotechnical characteristics, were reconstructed based on laboratory analysis and previously published work at the site (**Frodella et al.,**

2021; **Domej et al., 2022**; **Gasbarrone, 2005**; **Margottini & Spizzichino, 2020**; **Shafiei & Dusseault, 2008**; **Bergamini, 2020**). A hybrid constitutive approach was adopted. The mechanical behavior of the sandstone unit was modeled using the generalized Hoek–Brown failure criterion (**Hoek et al., 2002**), which is appropriate for representing the strength and deformability of fractured rock masses. The Uniaxial Compressive Strength of the sandstone intact rock (UCS) was set to 14 MPa based on field-based classification schemes and literature values consistent with moderately cemented, weak sandstones. Although laboratory tests on specimens by **Domej et al. (2022)** yielded much lower UCS values ($\approx 0.85MPa$), these were not considered representative of the competent rock mass forming the vertical cliffs and carved cavities of the Sabereebi site since laboratory tests were conducted in weathered samples.

The Geological Strength Index (GSI) was set equal to 60 based on in situ observations and the graphical GSI chart embedded in RS3, which follows the classification scheme of **Marinos & Hoek (2000)**. This GSI value corresponds to a rock mass described as "intact or massive – intact rock specimens or massive in situ rock with few widely spaced discontinuities", with fair surface conditions. This classification was supported by field observations and photointerpretation of photographs from the UAV and TLS surveys, which revealed moderate jointing and good block interlocking, consistent with a relatively undisturbed sandstone mass.

The material constant for intact rock (*mi*) was set to 17 as selected from the material property RS3 database, where it is listed as the representative value for moderately strong, quartz-rich sandstones. This value reflects typical intact strength behavior and is consistent with the empirical recommendations by **Hoek et al. (2002)** taking into consideration the rock type, mineralogy, grain size, and cementation.

A disturbance factor (D) of zero was applied, as no disturbance (e.g., blasting) was performed and the rock is considered to be in its natural, undisturbed condition. In addition, a tensile strength cut-off of 0.05 MPa was adopted from **Domej et al. (2022)**,

representing the tensile stress threshold beyond which brittle failure initiates.

All the previous parameters were implemented in RS3 software using the generalized Hoek–Brown formulation (**Hoek et al., 2002**), which internally converts them to an equivalent Mohr–Coulomb envelope for the simulation of progressive failure in the fractured sandstone.

In Table 3.18, input values considered for the sandstone parameters are summarized.

Table 3.18: Parameters assigned to the sandstone unit modelled with the generalized Hoek–Brown criterion (**Hoek et al., 2002**).

Material unit	**UCS (MPa)**	**GSI**	m_i	D	**Tensile strength cut-off (MPa)**
Sandstone	14	60	17	0	0.05

The other lithological units present in the model, such as topsoil, conglomerate, clay, and siltstone, were modeled using the Mohr-Coulomb failure criterion (**Coulomb, 1776**), which assumes a linear relationship between shear strength and normal stress. This approach was deemed appropriate for materials that either lack sufficient engineering-geological data to support a nonlinear strength envelope or exhibit predominantly ductile or homogeneous behavior under load.

The Mohr-Coulomb model also allows for a straightforward assignment of peak strength parameters such as friction angle (ϕ) and cohesion (c), which were derived from a combination of laboratory testing, field classification, and literature references (**Domej et al. 2022**; **Gasbarrone, 2005**; **Margottini & Spizzichino, 2020**; **Shafiei & Dusseault, 2008**). These materials do not exhibit the degree of fracturing or scale-dependent strength degradation that would require a nonlinear criterion like Hoek–Brown (**Hoek et al., 2002**), and their strength parameters are considered to remain approximately constant under the range of confining stresses modeled. For this reason, the Mohr-Coulomb model provides a practical and sufficiently accurate representation of their mechanical behavior within the FEM simulation. In Table 3.19, are summarized the geoptechnical parameters used.

Table 3.19: Geotechnical parameters chosen as input for the FEM simulation (Mohr–Coulomb = MC; Generalized Hoek–Brown = GHB).

Layer	**Behaviour**	E **(MPa)**	ν **(–)**	γ **(MN/m^3)**	φ **(°)**	c **(MPa)**
Topsoil	MC	1.1	0.3	0.0180	21.5	0.025
Conglomerate	MC	5000	0.3	0.0204	31.5	3.500
Sandstone	GHB	155	0.2	0.0165	42.0	0.150
Siltstone	MC	285	0.2	0.0158	42.0	0.150
Clay	MC	125	0.3	0.0192	20.5	0.020

As regards the rock fractures, in the absence of direct in situ or laboratory testing, the Joint Wall Compressive Strength (JCS) was estimated indirectly from the Uniaxial Compressive Strength (UCS) of the intact sandstone, following the assumption proposed by **Bandis et al. (1983)**; the assumption considers the JCS approximately equal to the UCS when specific measurements are not available. Field observations at Sabereebi indicate that the sandstone forms stable vertical walls and vaulted cavities, with moderate cementation and surface weathering. Based on visual classification and the field-based strength categories of **Hoek & Brown (1997)**, the rock was classified as a "weak rock" (R2), with a UCS ranging between 5 and 25 MPa. A representative average of UCS equal to 14 MPa was adopted, and the same value was assigned to JCS, reflecting the expected compressive strength of joint wall material in its moderately weathered state.

The Joint Roughness Coefficient (JRC) was set equal to 5, based on qualitative field observations of the joint surfaces within the sandstone. The discontinuities exhibit undulating geometries and moderate roughness, without significant interlocking or step features. This estimate falls within the empirically defined range of **Barton & Choubey (1977)** for moderately rough joints.

The residual friction angle (ϕr) was set to 33°, in accordance with the same empirical framework **Barton & Choubey (1977)**. Assuming a peak friction angle of 42°, consistent with the Mohr–Coulomb parameters assigned to intact sandstones, the residual

value accounts for post-failure conditions characterized by reduced surface roughness and mechanical interlocking. This estimate is consistent with values typically reported for moderately rough joints in weakly cemented sedimentary rocks under dry conditions and ensures compatibility with the non-linear shear strength formulation implemented in the Barton–Bandis model.

Also, the initial stiffness properties were assigned based on empirical relationships: according to **Bandis et al. (1983)**, the normal stiffness k_n was scaled proportionally to JCS using an empirical order-of-magnitude factor (≈ 10) suitable for closed, unfilled sedimentary joints when no joint closure stiffness tests exist, consistently with the dependency of initial joint normal stiffness on joint wall strength reported in Barton's and Bandis' empirical joint model framework. Therefore, the normal stiffness k_n was approximated following the formula:

$$k_n \approx 10 \times \text{JCS} \ (\text{MPa/m}) \tag{3.3}$$

Given the assigned value of JCS equal to 14 MPa, a value of k_n equal to 140 MPa/m was used to reflect a rock-mass response consistent with field observations of closed, undulating discontinuities. Experimental studies on natural rock joints indicate that the shear stiffness is significantly lower than the normal stiffness, without defining a unique ratio (**Barton & Choubey, 1977**; **Bandis et al., 1983**). In numerical modelling, explicit stiffness values are required; therefore, the shear stiffness k_s was assumed as a fraction of the normal stiffness. Based on documented numerical modelling practice and RS3 joint verification benchmarks, a representative value was adopted as follows:

$$k_s \approx 0.2\, k_n = 0.2 \times 140 = 28 \ \text{MPa/m} \tag{3.4}$$

In Table 3.20, the input values considered for joint parameters are summarized.

Table 3.20: Summary of the assigned joint parameters according to the Barton–Bandis model (**Barton & Bandis, 1990**).

Parameter	**Assigned value**
JRC (–)	5
JCS (MPa)	14
φ_r (°)	33
k_n (MPa/m)	140
k_s (MPa/m)	28

Figure 3.29 illustrates the three-dimensional finite element model built in RS3 software to simulate the engineering-geological behavior of the Sabereebi Monastic Complex and its hosting slope. The model incorporates site-specific stratigraphy, internal cavities, and key structural discontinuities based on integrated geomatic and engineering-geological data interpretation.

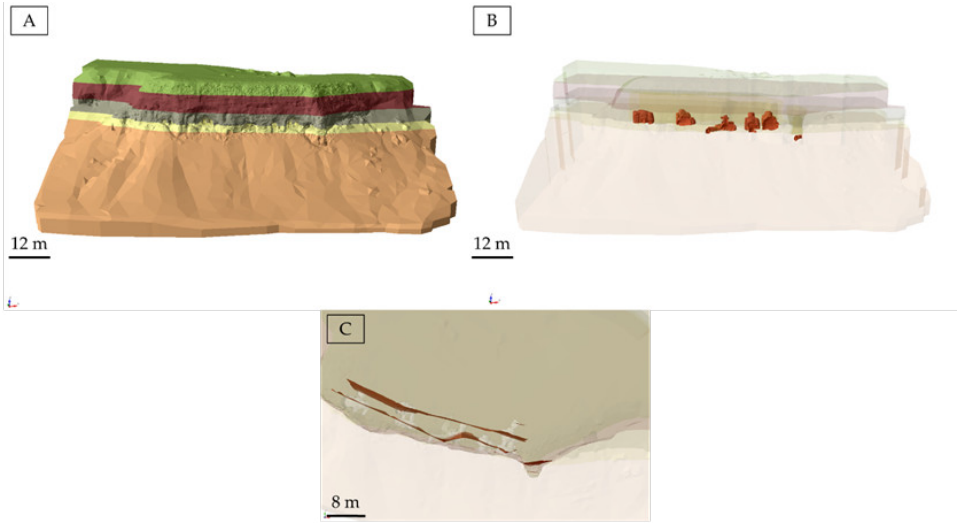

Figure 3.29: Three-dimensional numerical model of the Sabereebi slope and monastic complex developed in RS3. Panel (A) shows the full stratigraphic model with lithological units differentiated by color: topsoil (green), conglomerate (dark red), sandstone (light grey), siltstone (light yellow), and clay (light brown). Panel B shows the internal cave chambers reconstructed from TLS and UAV photogrammetric data and integrated as excavated voids within the sandstone. Panel C shows the planar discontinuities inserted into the sandstone unit based on field observations and 3D interpretation.

Panel A of Figure 3.29 emphasizes the geological framework of the slope and the vertical extent of the sedimentary sequence, which controls the spatial distribution of material properties within the model domain.

Panel B shows the internal geometry of the cave system, reconstructed from high-resolution TLS and UAV-based photogrammetric surveys. The volumes corresponding to the rock-cut chambers—such as chapels, monastic cells, and connecting corridors—were manually modeled and integrated as excavated voids within the sandstone unit. These are highlighted in reddish brown and represent the central architectural features of the monastic complex.

In panel C, the main joint sets observed in the field are explicitly inserted as planar discontinuities within the sandstone. Their orientations, spacing, and persistence were derived from a combination of structural field surveys and 3D photointerpretation.

The combination of lithological heterogeneity, architectural excavation, and structural anisotropies helps to capture the model key factors influencing stability at Sabereebi, providing a realistic foundation for subsequent numerical analysis interpretation.

3.2.5 Results

3.2.5.1 Point cloud processing

Digital photogrammetric techniques implemented in Agisoft^{TM} Metashape were used to align the 383 images acquired during the UAV 2025 campaign. The processing identified approximately 237,907 matching keypoints. The alignment of photographs yielded an RMSE of 5.38 cm. The final dense point cloud consisted of about 74 million 3D points, later interpolated to produce a high-resolution Digital Dense Elevation Model (DDEM) with a spatial resolution of 2.31 cm/pixel. Using this model, the original images were geometrically corrected and mosaicked to create an orthophotomosaic including both nadiral and oblique views. The spatial resolution of the orthophotomosaic is 1.16 cm/pixel. All

photogrammetric products were georeferenced in the WGS84/UTM Zone 38N coordinate system (EPSG:32638).

As regards the 2025 TLS, the final RMSE of scans registration, after editing and georeferencing, is equal to 7.14 mm, confirming high alignment precision. For enhanced visualization and structural photointerpretation, TLS point clouds were colorized using the RealColor tool in Trimble^{TM} RealWorks. This was achieved by projecting high-resolution panoramic images acquired with the Nikon D7100 digital camera onto the 3D geometry. The integration of the final TLS point cloud with that from UAV survey required an additional registration step, producing an inter-dataset registration error of 30.49 mm that can be considered sufficiently accurate for combined structural and geomorphological analysis. In the following Figure 3.30 the point clouds obtained from the 2025 TLS and UAV, after processing and segmentation considering the area of interest, are shown in panel A and B, respectively.

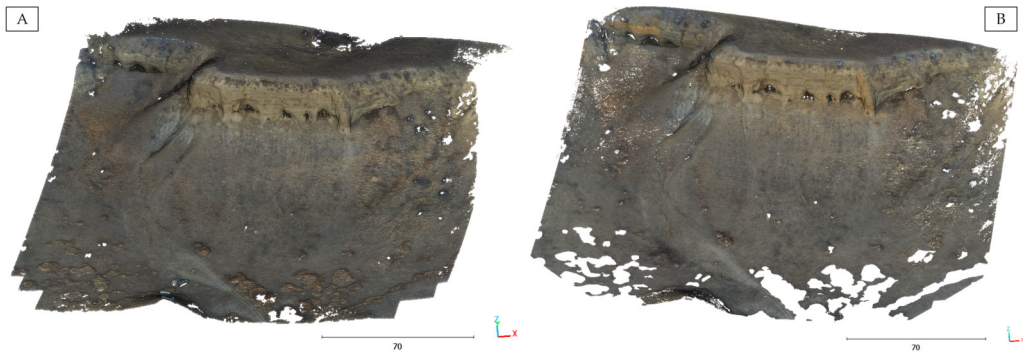

Figure 3.30: Panel A shows the segmented point cloud obtained by processing the TLS data, while panel B shows the point cloud obtained from UAV photogrammetry. Both point clouds are segmented considering the area of interest.

Before export, the final complete registered 3D point cloud was uniformly resampled in Trimble^{TM} Scan Explorer following a variable-resolution strategy: primary areas of interest (caves and adjacent slope) were downsampled to 2 cm spacing, while peripheral surrounding areas were reduced to 50 cm to optimize file size. Data were exported in `*.las` format and processed in CloudCompare for filtering and mesh preparation. Noise

reduction was performed through a combination of automated and manual techniques. The *Statistical Outlier Removal* (SOR) filter eliminated sparse noise based on local point density (**CloudCompare, 2021**); the *Colorimetric Segmenter* allowed to remove vegetation (**Collier et al., 2020**), while the *Cloth Simulation Filter* (CSF) identified the ground by simulating a virtual cloth draped over the inverted point cloud: the cloth conforms to the terrain surface, allowing ground points to be separated from vegetation and other above-ground elements (**Zhang et al., 2016**). These CloudCompare tools are useful to clean clouds from elements (e.g., vegetation, scaffoldings, objects) which could create artifacts in the 3D model. Manual refinement further corrected residual artifacts. The cleaned dataset, containing approximately 4.4 million points, was re-imported into Agisoft™ Metashape to generate surface meshes for the slope and each cave chamber. These meshes were exported in `*.obj` format before undergoing topological cleaning (removal of non-manifold edges, degenerate triangles, and mesh overlaps) to ensure compatibility and numerical stability within the Rocscience™ RS3 (Version 4.039; **Rocscience™ Inc. 2025**) FEM modeling environment. The final mesh is composed by more than 515,000 faces.

3.2.5.2 Surface change detection from multitemporal point cloud comparison

The analysis served as a preliminary diagnostic tool to identify active areas of erosion and deformation, guiding structural mapping and stability modeling. The registration error between the 2018 and the 2025 point clouds, as computed by the M3C2 algorithm in CloudCompare (**CloudCompare, 2021**), resulted equal to 37 mm. This value was subsequently adopted as input parameter for the registration uncertainty in the surface change detection. The comparison revealed 11 localized surface retreat primarily along the vertical cliff face hosting the cave entrances. Quantitative 3D displacement data indicated distinct zones of material loss and minor detachment, concentrated around structurally weakened or highly weathered outcrops.

By quantifying the magnitude and spatial distribution of change between epochs,

the analysis provided valuable insight into areas undergoing progressive degradation or instability.

The volumetric assessment of the eleven identified detachment features revealed a sharp contrast in the magnitude of material loss across the façade (Figure 3.31, Table 3.21).

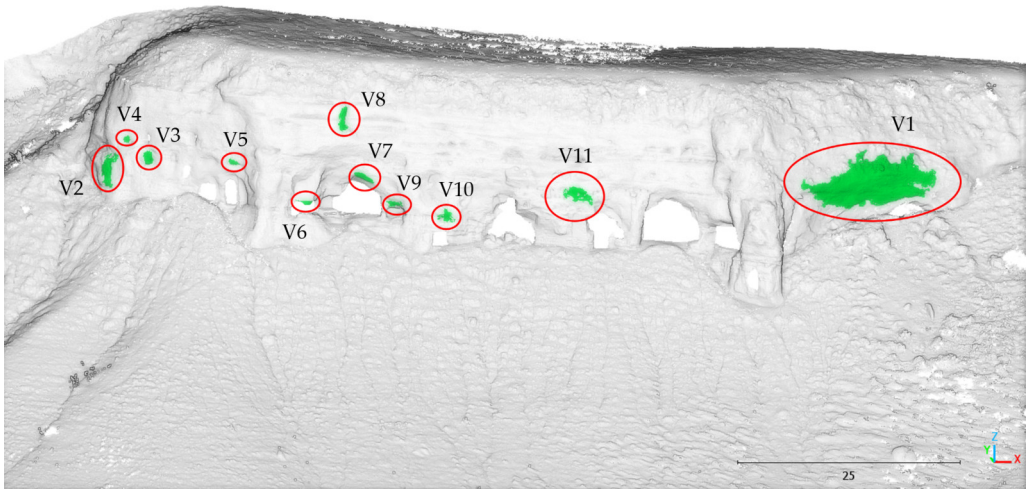

Figure 3.31: Results of the M3C2 analysis between 2018 and 2025 point clouds. Colored in green and indicated by red the blocks and detachment areas are shown.

While most detachments correspond to small-scale granular disaggregation (volumes < 0.99 m^3 – See Table 3.21), a single large collapse located in the eastern sector of the cliff dominates the cumulative mass loss. This feature (named V1 in Table 3.21 and Figure 3.31) accounts for 31.44 m^3 of detached material and represents a significant localized retreat affecting the structural integrity of the overhanging portion of the façade. This volume is in correspondence with one of the joints mapped and shown in Figure 3.28, Panel C.

The remaining detachments range between 0.05 and 0.99 m^3, reflecting progressive weathering and small block removals along pre-existing discontinuities. The spatial clustering of blocks 2–11 around the cave entrances and carved architectural surfaces

indicates a preferential weakening of anthropically modified zones, where the removal of supporting rock most probably reduced the residual stability of the façade Figure 3.31.

Table 3.21: Volumes of detached material between 2018 and 2025 derived from M3C2-based segmentation and *Poisson Surface Reconstruction*.

Detachment ID	**Volume (m^3)**
V1	31.44
V2	0.99
V3	0.35
V4	0.05
V5	0.05
V6	0.25
V7	0.09
V8	0.28
V9	0.12
V10	0.12
V11	0.26

These volumetric data confirm that degradation at Sabereebi is characterized by a dual failure mechanism: (i) large but infrequent collapses driven by discontinuity-controlled slab detachment (e.g., V1), and (ii) persistent micro-scale weathering processes leading to incremental façade recession and diffuse surface retreat.

3.2.5.3 FEM modeling for slope stability analysis

The FEM simulations provided a detailed assessment of how the Sabereebi cliff and its rock-cut chambers redistribute stresses and undergo deformation under the current geological and structural configuration. Given the heterogeneous and stratified nature of the sedimentary units, the presence of discontinuities, and the strong geometric influence of the carved cavities, the interpretation focuses on stress and displacement parameters that robustly describe the mechanical response of the cliff and cavities.

For this reason, the analysis of results concentrates on three key outputs: (i) the major principal stress (σ_1), which identifies zones of compressive stress concentration and highlights how the excavated volumes redirect load paths within the rock mass; (ii) the